LETTER

Reconstruction and control of a time–dependent two–electron wave packet

Christian Ott[1]†, Andreas Kaldun[1], Luca Argenti[2], Philipp Raith[1], Kristina Meyer[1], Martin Laux[1], Yizhu Zhang[1], Alexander Blättermann[1], Steffen Hagstotz[1], Thomas Ding[1], Robert Heck[1], Javier Madroñero[3]†, Fernando Martín[2,4] & Thomas Pfeifer[1,5]

The concerted motion of two or more bound electrons governs atomic[1] and molecular[2,3] non-equilibrium processes including chemical reactions, and hence there is much interest in developing a detailed understanding of such electron dynamics in the quantum regime. However, there is no exact solution for the quantum three-body problem, and as a result even the minimal system of two active electrons and a nucleus is analytically intractable[4]. This makes experimental measurements of the dynamics of two bound and correlated electrons, as found in the helium atom, an attractive prospect. However, although the motion of single active electrons and holes has been observed with attosecond time resolution[5–7], comparable experiments on two-electron motion have so far remained out of reach. Here we show that a correlated two-electron wave packet can be reconstructed from a 1.2-femtosecond quantum beat among low-lying doubly excited states in helium. The beat appears in attosecond transient-absorption spectra[5,7–9] measured with unprecedentedly high spectral resolution and in the presence of an intensity-tunable visible laser field. We tune the coupling[10–12] between the two low-lying quantum states by adjusting the visible laser intensity, and use the Fano resonance as a phase-sensitive quantum interferometer[13] to achieve coherent control of the two correlated electrons. Given the excellent agreement with large-scale quantum-mechanical calculations for the helium atom, we anticipate that multidimensional spectroscopy experiments of the type we report here will provide benchmark data for testing fundamental few-body quantum dynamics theory in more complex systems. They might also provide a route to the site-specific measurement and control of metastable electronic transition states that are at the heart of fundamental chemical reactions.

Electrons are bound to atoms and molecules by the Coulomb force of the nuclei. Moving between atoms, they form the basis of the molecular bond. The same Coulomb force, however, acts repulsively between the electrons. This electron–electron interaction represents a major challenge in the understanding and modelling of atomic and molecular states, their structure and in particular their dynamics[2,3,14]. Here we focus on the ^{1}P $sp_{2,n+}$ series[15] of doubly excited states in helium below the $N = 2$ ionization threshold. They are produced through a single-photon-induced transition of both electrons of the ^{1}S $1s^2$ ground state to at least principal quantum number $n = 2$, and autoionize as a result of electron–electron
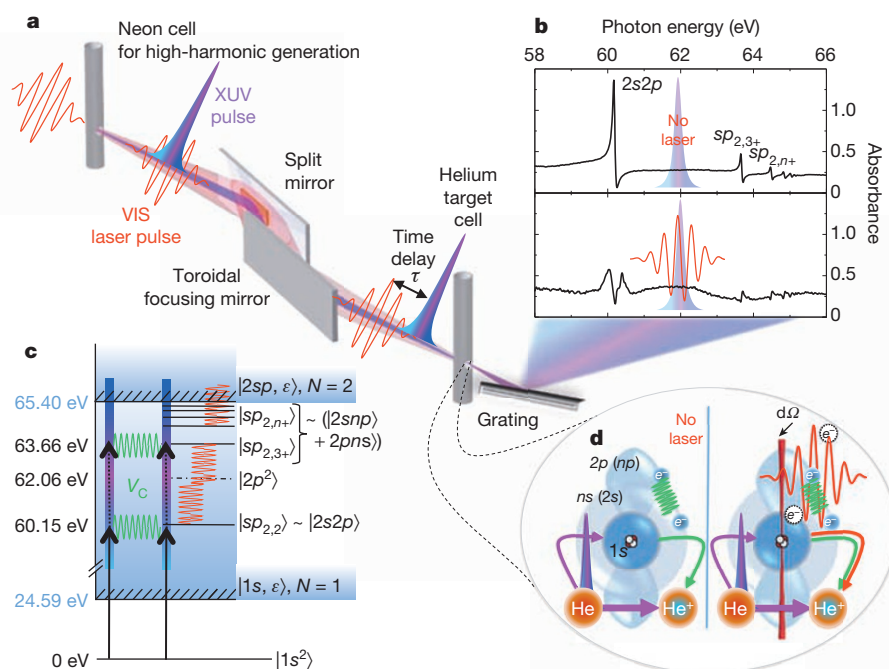

Figure 1 | Experimental set-up, data and microscopic mechanisms in helium. **a**, Few-cycle (7 fs) VIS laser pulses (730 nm) are focused into a neon gas cell for partial attosecond-pulse conversion, providing a continuous coherent excitation spectrum throughout the XUV range. The time delay between the co-propagating VIS and XUV pulses is controlled by a split-mirror stage. Both pulses transit the helium gas target and enter the high-resolution spectrometer. **b**, Absorption spectra without (upper) and in the presence of (lower) the VIS laser pulse, in the region of the $|sp_{2,n+}\rangle$ doubly excited states. **c**, Helium level diagram. The $|sp_{2,n+}\rangle$ states couple (indicated by green wavy lines) to the $|1s,\varepsilon p\rangle$ continuum by configuration interaction V_{CI}. The VIS laser field (red wavy lines) creates an additional time- and intensity-dependent coupling. **d**, The XUV pulses can either directly ionize He to He$^+$, or excite both electrons into an intermediate transition state, which decays by configuration interaction V_{CI} into He$^+$, quantum-interfering with the direct ionization process (left; natural process). If a laser field is present (right), it shifts the phase of one arm of this natural interferometer—the two-electron transition state—modifying the Fano line shapes detected in the transmitted absorption spectrum. This provides state-resolved experimental access to a quantum phase shift.

[1]Max-Planck-Institut für Kernphysik, Saupfercheckweg 1, 69117 Heidelberg, Germany. [2]Departamento de Química, Módulo 13, Universidad Autónoma de Madrid, 28049 Madrid, Spain. [3]Physik-Department, Technische Universität München, 85747 Garching, Germany. [4]Instituto Madrileño de Estudios Avanzados en Nanociencia, Cantoblanco, 28049 Madrid, Spain. [5]Center for Quantum Dynamics, Ruprecht-Karls-Universität Heidelberg, 69120 Heidelberg, Germany. †Present address: Chemistry Department, University of California, Berkeley, California 94720, USA (C.O.); Departamento de Física, Universidad del Valle, A.A. 25360, Cali, Colombia (J.M.).

interaction. Spectroscopically, the signature of these states is a Fano profile, an asymmetric non-Lorentzian line shape first observed in the 1930s[16] and attributed[17] to the quantum interference of bound states with the continuum to which they are coupled (Fig. 1c, d). The coupling is described by the configuration interaction V_{CI} with the single-ionization continuum $|1s, \varepsilon p\rangle$, where one electron is in the $1s$ ground state and the other one is in the continuum with kinetic energy ε. The magnitude of V_{CI} determines the lifetimes of the transiently bound states, which in our case range between 17 fs for the $2s2p$ (denoted $sp_{2,2}$) state[18] and several hundreds of femtoseconds for some higher-lying $sp_{2,n+}$ states[15]. Such short lifetimes, together with the fast dynamics caused by energy-level spacings on the order of several electronvolts demand ultrashort laser pulses for measuring the coupling dynamics between the states in external fields. Previous time-resolved experiments observed the light-induced modification of absorption profiles[8], or used attosecond streak-field spectroscopy[18] to measure the $2s2p$ autoionization lifetime. A 1.2 fs two-electron wave packet formed by the coherent superposition of two autoionizing states was recently predicted theoretically[19].

Our experimental method (Fig. 1a, b, 'Experimental apparatus details' and 'Experimental data acquisition' in Methods, and Extended Data Fig. 1) combines the attosecond transient-absorption scheme and an extreme-ultraviolet (XUV) flat-field grating spectrometer with high-spectral-resolution capability. It allows the parallel measurement of spectrally narrow absorption lines imprinted on an attosecond-pulsed broadband XUV spectrum in the presence of a near-visible (VIS) laser

field. The VIS laser couples the two-electron excited states (Fig. 1c) either weakly, when operated at low intensities, or strongly, when operated at high intensities. The time delay between the VIS and XUV fields and the intensity of the VIS field are varied independently to create a multidimensional transient-coupling scheme that is based on the perturbed free polarization decay and is well known from femtosecond transient-absorption studies[20]. To complement the experiments, we also performed *ab initio* theoretical calculations of the attosecond transient-absorption spectra and the two-electron wave-packet motion of the helium atom in a laser field using state-of-the-art methods for integrating the time-dependent Schrödinger equation on a fully correlated two-electron close-coupling configuration basis ('*Ab initio* TDSE simulation' in Methods).

In Fig. 2, we compare the differential absorption spectra, for varying VIS–XUV time delays and a low VIS intensity of 3×10^{10} W cm^{-2}, obtained from experiment (Fig. 2a), few-level model simulations (Fig. 2b; 'Few-level model simulation' in Methods and Extended Data Fig. 2) and *ab initio* calculations (Fig. 2c). We note the excellent agreement between the results, which gives confidence that we can fully understand the dynamics probed in this study. The time-resolved absorption change occurring near the two lowest-lying states, $2s2p$ and $sp_{2,3+}$, appears after zero time delay in the form of temporally oscillating structures with a period of ~1.2 fs, indicating coherent two-electron wave-packet dynamics that has been initiated by the XUV pulse and is probed by coupling with the weak VIS pulse. The few-level model confirms the probing mechanism as VIS-induced two-photon dipole coupling of the $2s2p$ and the $sp_{2,3+}$
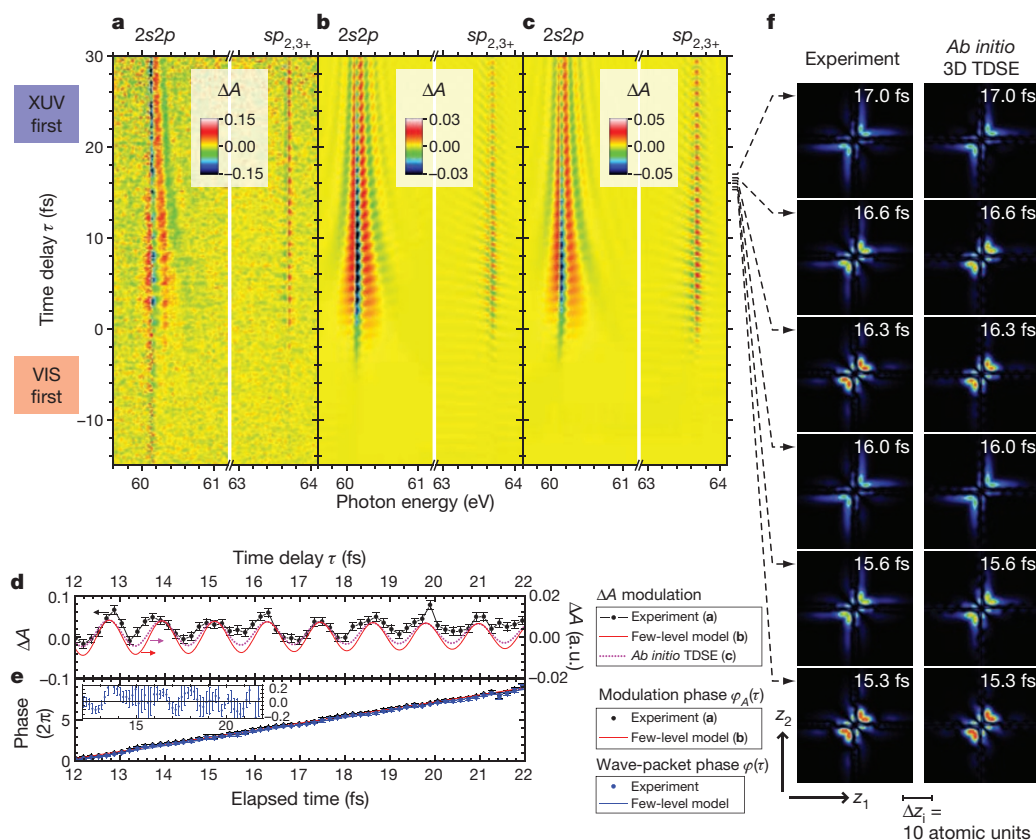

Figure 2 | Observation of attosecond two-electron dynamics in helium.
a–c, Absorbance change (ΔA) of XUV light in helium versus time delay between the VIS (3×10^{10} W cm^{-2} intensity) coupling field and the XUV pulse: experiment (**a**), few-level model simulation (**b**; ΔA in arbitrary units) and *ab initio* calculation (**c**; ΔA in arbitrary units) show the onset of temporal oscillations near time delay $\tau = 0$ and persisting to large positive delays. **d**, Oscillation of ΔA (arbitrary units, a.u.) versus τ near resonance at 63.67 eV. **e**, Modulation phase $\varphi_A(\tau)$ of $\Delta A(\tau)$ and relative phase $\varphi(t)$ of the XUV-pulse-induced two-electron wave packet involving the $2s2p$ and $sp_{2,3+}$ states, reconstructed by applying to $\varphi_A(\tau)$ a small systematic phase shift ('Measuring the wave-packet phase in real/elapsed time' in Methods). The inset shows the

experimentally retrieved phase $\varphi(t)$ relative to the theoretical expectation. The error bars in **d** and **e** reflect the statistical noise (s.d.) of the measured absorption spectra. **f**, Visualization of the two-electron wave-packet motion. Snapshots of the correlated quantum probability distribution along a line (within infinitesimal cone dΩ, see Fig. 1d) through the helium atom are shown at several instants of elapsed time t. Left column, experimentally reconstructed wave packet including only the two measured states $2s2p$ and $sp_{2,3+}$. Right column, *ab initio* simulation of the three-dimensional time-dependent Schrödinger equation (TDSE), including all excited states. 1 atomic unit = 0.529 Å.

states proceeding via the energetically intermediate and spectroscopically dark $2p^2$ state at 62.06 eV (Fig. 1c). Although the $2s2p \leftrightarrow 2p^2$ transition alone was previously used to control the transmission of helium[8,12,18], here we measure and exploit the coupling of three autoionizing states to reconstruct the two-electron wave packet.

The approximate time-dependent wavefunction

$$|\Psi(t)\rangle \propto \exp\left(-\frac{\Gamma_{2s2p}}{2}t\right)|2s2p\rangle$$
$$+ a \, \exp\left(-\frac{\Gamma_{sp2,3+}}{2}t\right)\exp[-i\varphi(t)]|sp_{2,3+}\rangle$$

is characterized by the relative phase $\varphi(t)$ and amplitude a of the two contributing states, $2s2p$ and $sp_{2,3+}$. The states' slow amplitude decay is given by their respective natural decay widths Γ, accessible from static spectroscopy[15]. The relative amplitude $a = (d_{sp2,3+}/d_{2s2p})$ $\sqrt{S(\omega_{sp2,3+})/S(\omega_{2s2p})}$ follows directly from the states' dipole moments d_{2s2p} and $d_{sp2,3+}$ between the doubly excited state and the ground state[21], and the XUV spectrum $S(\omega)$ at the resonance positions ω_{2s2p} and $\omega_{sp2,3+}$. The relative phase $\varphi(t)$ by contrast is not accessible using traditional spectroscopy. In our time-resolved measurement, different transition pathways involving the doubly excited states interfere as a function of time, allowing us to turn $\varphi(t)$ into an experimental observable by analysing the delay-dependent near-resonance absorption ('Measuring the wave-packet phase in real/elapsed time' in Methods and Extended Data Figs 5 and 6). The measured phase $\varphi(t)$ is plotted in Fig. 2d, e, and agrees well with the *ab initio* simulation results. The relative amplitude is given by $a = 0.5 \pm 0.2$, where the error is mainly due to the fluctuation of the experimental XUV spectrum. The measured values of a and $\varphi(t)$ fully characterize the two-electron wave packet composed of the two auto-ionizing quantum states $|2s2p\rangle$ and $|sp_{2,3+}\rangle$, which we can reconstruct and visualize by using the known time-independent real-space representations of these states calculated by the complex scaling method[22]. Figure 2f compares a section of the reconstructed time-dependent spatial distribution of the two electrons against *ab initio* time-dependent simulation, showing very good agreement and that the main features of the two-electron dynamics are thus dominated by the superposition of the $|2s2p\rangle$ and $|sp_{2,3+}\rangle$ states. Owing to the well-defined spectral coherence (that is, phase locking[23]) present in a high-harmonic spectrum, the observation of a well-defined phase evolution $\varphi(t)$ is possible[24] even in the absence of carrier-envelope phase stabilization and without knowing the number of attosecond pulses in the few-cycle attosecond-pulse train that we generate ('Effects of the attosecond pulse configuration and the carrier envelope phase' in Methods and Extended Data Figs 4–6). We note that the images in Fig. 2f clearly show that the two-electron motion in the reconstructed doubly excited wave packet is highly correlated, although direct experimental observation of such concerted dynamics would require coincidence techniques[25–27] and represents a major future goal.

The spectra obtained with a higher VIS intensity of $3.5 \times 10^{12}\,\mathrm{W\,cm^{-2}}$ from both experiment (Fig. 3a) and *ab initio* simulations (Fig. 3b) show a shifting, splitting and broadening of the main absorption lines near zero delay, as previously documented in inner-valence excitations of argon[9]. The wave-packet motion is still present and seen as fast absorbance modulations even at late delay times, but is significantly affected by the more intense VIS pulse. Near zero delay time, we also observe strong delay-dependent modifications of the Fano spectral line shapes of the higher-lying states, again with remarkable agreement between the experimental data and the *ab initio* simulation.

After measuring the time-dependent relative phase of quantum states in a two-electron wave packet, we use our experimental method for general two-electron quantum-state holography and wave-packet control. Here the electric field strength of the VIS pulse is an important parameter: it controls the coupling strengths between the states and between the states and the continuum. Continuous variation of the VIS pulse intensity thus opens a third spectroscopic dimension (Supplementary

Video 1), in addition to the time delay and the spectrum. This is illustrated in Fig. 4a, where tuning of the VIS laser intensity at a fixed time delay of 5.4 fs continuously maps the transition from the unperturbed regime to the strong-coupling regime of discrete, doubly excited states that is evident near 60 eV. All states are observed to resist the laser electric fields far beyond classical detachment of the outermost electron by overcoming the attractive nuclear Coulomb force (over-the-barrier ionization[28]).

We also observe, for all states, a continuous change in the Fano line shape as a function of intensity. Because the line shape of such laser-modified Fano resonances contains information on the phase of the complex dipole response function $d(t)$ after the interaction with the VIS laser pulse[13], whereas the $1s^2$ ground state is not significantly affected by the VIS laser at the intensities used here, we can use

$$d_n(t) \propto \langle 1s^2|d|sp_{2,n+}\rangle\exp(-iE_n t)\exp(i\phi_n)$$

to extract the dipole phase shift ϕ_n that is approximately equal to the relative phase shift φ_n of the quantum state at energy E_n. The phase changes of the $2s2p$ and $sp_{2,3+}$ states reconstructed in this way are shown in Fig. 4c, d. The excellent agreement between ϕ_n (extracted from the Fano line shape[13]) and φ_n (defining the wave packet) confirmed by the *ab initio* simulation in Fig. 4b, e, f validates our strategy of experimentally mapping out the intensity-dependent phase shifts $\varphi_n(I)$ of the quantum states by analysing the Fano line shapes ('Line-shape analysis for
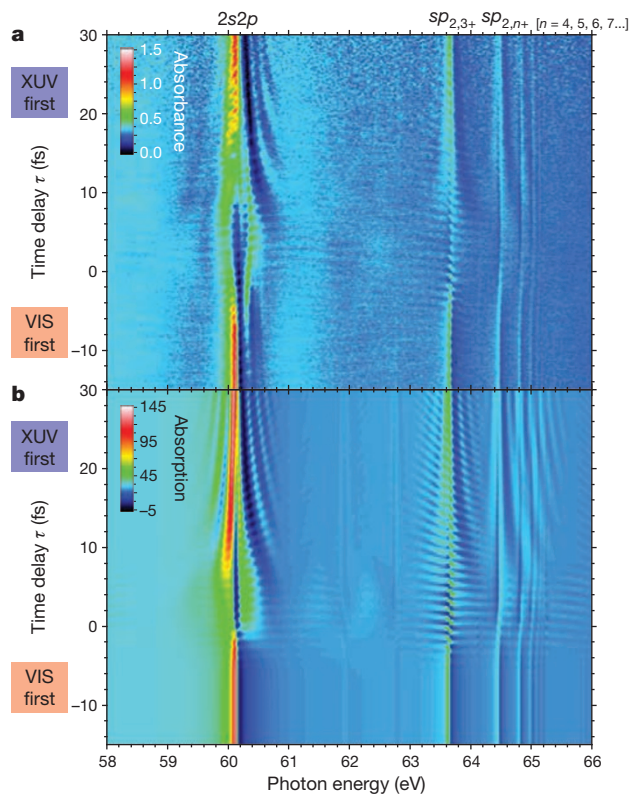

Figure 3 | Time-delay-dependent absorption at higher VIS intensity ($3.5 \times 10^{12}\,\mathrm{W\,cm^{-2}}$). a, Time-resolved experimental absorption spectrum at a higher VIS intensity of $3.5 \times 10^{12}\,\mathrm{W\,cm^{-2}}$. At negative delays, the static Fano profile[17] is measured for several autoionizing states up to $sp_{2,7+}$. Near temporal overlap and at positive delays, the absorption spectrum is strongly modified. At slightly positive delays, a clear signature of Autler–Townes splitting of the $2s2p$ resonance with the energetically repelling $2p^2$ dressed state is measured at ~60 eV, confirming the strong-coupling regime of autoionizing states and multiple Rabi cycling between these two states. **b,** The full *ab initio* simulation (absorption in arbitrary units) shows excellent agreement with the experiment, thus providing further proof of the existence of a well-defined two-electron wave packet even at higher VIS intensities.
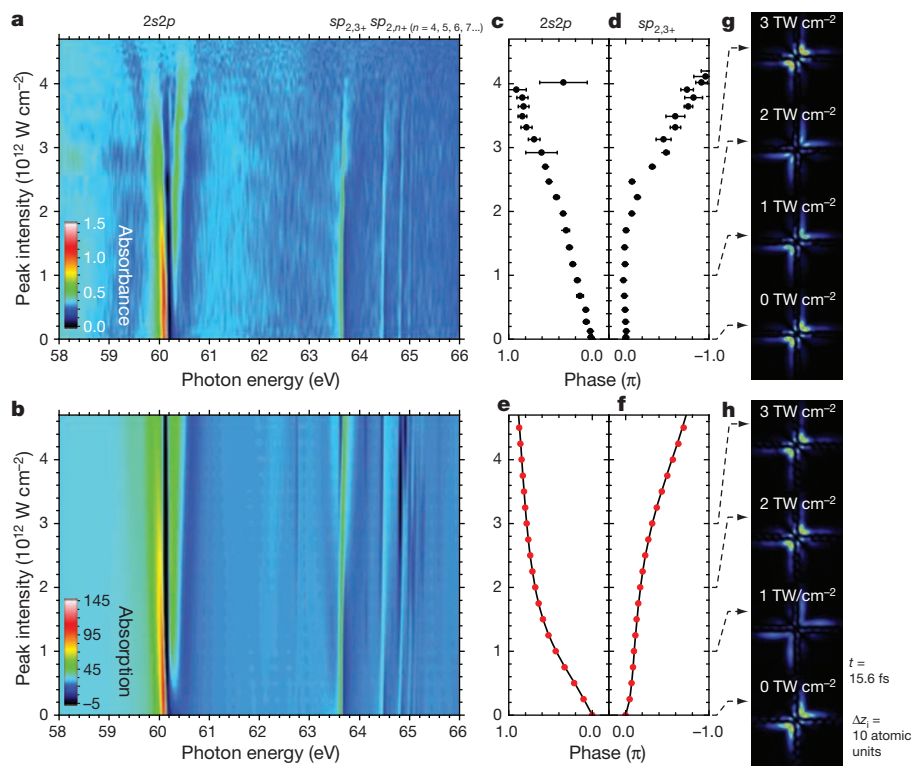
a 2s2p $sp_{2,3+}$ $sp_{2,n+}$ (n = 4, 5, 6, 7...) **c** 2s2p **d** $sp_{2,3+}$ **g** 3 TW cm^{-2}

Peak intensity (10^{12} W cm^{-2})

Absorbance 1.5 1.0 0.5 0.0

58 59 60 61 62 63 64 65 66
Photon energy (eV)

Phase (π) 1.0 0.0 0.0 −1.0

2 TW cm^{-2}

1 TW cm^{-2}

0 TW cm^{-2}

b **e** **f** **h** 3 TW cm^{-2}

Peak intensity (10^{12} W cm^{-2})

Absorption 145 95 45 −5

58 59 60 61 62 63 64 65 66
Photon energy (eV)

Phase (π) 1.0 0.0 0.0 −1.0

2 TW cm^{-2}

1 TW/cm^{-2}

0 TW cm^{-2}

t = 15.6 fs

Δz_i = 10 atomic units

Figure 4 | Intensity-dependent laser coupling and phase control of a two-electron wave packet. a, XUV absorption spectra at a time delay of +5.4 fs for increasing VIS coupling intensity. Near 60 eV, we continuously follow the transition from the unperturbed regime to the two-electron strong-coupling regime of the $2s2p$ with $2p^2$ and $sp_{2,3+}$. **b,** Absorption spectra (arbitrary units) calculated using the *ab initio* simulation, as a function of the VIS intensity at a time delay of +4.8 fs. **c, d,** Reconstruction of the intensity-dependent temporal phase change of the $2s2p$ (**c**) and $sp_{2,3+}$ (**d**) states after their interaction with the VIS pulse, retrieved via Fano line-shape analysis[13] ('Line-shape analysis for phase retrieval' in Methods and Extended Data Fig. 7). The state-dependent change of the phase as a function of the intensity

demonstrates laser-controlled manipulation of the two-electron dynamics (**g**), shown in two-dimensional representation at a representative time t = 15.6 fs after the XUV pulse. **e, f,** Reconstruction of the intensity-dependent phase change in the *ab initio* simulation for the same states as in **c** and **d**, again using Fano line-shape analysis (black solid line). The red dots mark the phase shift of the coefficients, read out after the laser pulse. The excellent agreement with the phase extracted from line-shape analysis (experimentally accessible observable) validates this phase-reconstruction method. **h,** Two-electron probability distribution as obtained from the *ab initio* simulation, for the same time and intensity parameters as in **g**.

phase retrieval' in Methods and Extended Data Fig. 7). Because the phase dependences of $2s2p$ and $sp_{2,3+}$ are opposite in sign, their phase difference can be tuned through ~2π, allowing for the full control of the two-state two-electron wave packet. From the measured laser-induced shift in the phase of each quantum state, we can visualize the shape of the wave packet at any time during its field-free evolution. In Fig. 4g, h, we show this for the representative real time t = 15.6 fs. The laser intensity can thus be varied to control the shape of correlated two-electron wave packets at a specific time. In future applications to covalently bound neutral molecules, the strong-field shaping of two-electron wave packets may be a powerful means of laser control of chemical reactions. This further motivates experiments employing coincidence imaging methods (for a review, see, for example, ref. 25) for direct measurements of the spatial shape of two- or multi-electron wave packets as a function of time in the attosecond domain.

The extracted state-dependent phases $\varphi_n(I)$ will give further insight into the coupling between two electrons and how they, collectively or cooperatively, acquire dynamical phases $\varphi_n(I) = \int \Delta E_n(t)\,\mathrm{d}t$ as a result of time-dependent and state (n)-dependent energy-level shifts $\Delta E_n(t)$ (for example Stark or Zeeman shifts) under external perturbation. Having state-resolved access to and control over the full quantum information—amplitude and phase—for two-electron excited states as a function of time and intensity, more fundamental questions can be addressed in the future. For example, how do two-electron transition states respond to field strengths ranging from the weak- to the strong-field limit? What are the dynamics and fate of doubly excited states at and before the onset

of ionization? What is the validity range of commonly used[8,18,28] single-active electron pictures for strong-field ionization of few-electron systems? The answers have important consequences for goals such as the creation of synthetic atomic quantum systems and exotic molecules using ultrashort, temporally tailored light fields[29], beyond the reaches of traditional chemistry.

Online Content Methods, along with any additional Extended Data display items and Source Data, are available in the online version of the paper; references unique to these sections appear only in the online paper.

1. Pisharody, S. N. & Jones, R. R. Probing two-electron dynamics of an atom. *Science* **303,** 813–815 (2004).
2. Vanroose, W., Martin, F., Rescigno, T. N. & McCurdy, C. W. Complete photo-induced breakup of the H$_2$ molecule as a probe of molecular electron correlation. *Science* **310,** 1787–1789 (2005).
3. Remacle, F. & Levine, R. D. An electronic time scale in chemistry. *Proc. Natl Acad. Sci. USA* **103,** 6793–6798 (2006).
4. Lin, C. D. Hyperspherical coordinate approach to atomic and other Coulombic three-body systems. *Phys. Rep.* **257,** 1–83 (1995).
5. Goulielmakis, E. *et al.* Real-time observation of valence electron motion. *Nature* **466,** 739–743 (2010).
6. Mauritsson, J. *et al.* Attosecond electron spectroscopy using a novel interferometric pump-probe technique. *Phys. Rev. Lett.* **105,** 053001 (2010).
7. Holler, M., Schapper, F., Gallmann, L. & Keller, U. Attosecond electron wave-packet interference observed by transient absorption. *Phys. Rev. Lett.* **106,** 123601 (2011).
8. Loh, Z. H., Greene, C. H. & Leone, S. R. Femtosecond induced transparency and absorption in the extreme ultraviolet by coherent coupling of the He 2s2p (^{1}P^o)

and 2p² (¹Sᵉ) double excitation states with 800 nm light. *Chem. Phys.* **350,** 7–13 (2008).

9. Wang, H. *et al.* Attosecond time-resolved autoionization of argon. *Phys. Rev. Lett.* **105,** 143002 (2010).

10. Lambropoulos, P. & Zoller, P. Autoionizing states in strong laser fields. *Phys. Rev. A* **24,** 379–397 (1981).

11. Themelis, S. I., Lambropoulos, P. & Meyer, M. Ionization dynamics in double resonance involving autoionizing states in helium: the effect of pulse shapes. *J. Phys. B* **37,** 4281–4293 (2004).

12. Chu, W. C., Zhao, S. F. & Lin, C. D. Laser-assisted-autoionization dynamics of helium resonances with single attosecond pulses. *Phys. Rev. A* **84,** 033426 (2011).

13. Ott, C. *et al.* Lorentz meets Fano in spectral line shapes: a universal phase and its laser control. *Science* **340,** 716–720 (2013).

14. Meyer, H. D., Manthe, U. & Cederbaum, L. S. The multi-configurational time-dependent Hartree approach. *Chem. Phys. Lett.* **165,** 73–78 (1990).

15. Schulz, K. *et al.* Observation of new Rydberg series and resonances in doubly excited helium at ultrahigh resolution. *Phys. Rev. Lett.* **77,** 3086–3089 (1996).

16. Beutler, H. Über Absorptionsserien von Argon, Krypton und Xenon zu Termen zwischen den beiden Ionisierungsgrenzen ²P₃²ᐟ⁰ und ²P₁²ᐟ⁰. *Z. Phys. A* **93,** 177–196 (1935).

17. Fano, U. Effects of configuration interaction on intensities and phase shifts. *Phys. Rev.* **124,** 1866–1878 (1961).

18. Gilbertson, S. *et al.* Monitoring and controlling the electron dynamics in helium with isolated attosecond pulses. *Phys. Rev. Lett.* **105,** 263003 (2010).

19. Argenti, L. & Lindroth, E. Ionization branching ratio control with a resonance attosecond clock. *Phys. Rev. Lett.* **105,** 053002 (2010).

20. Pollard, W. T. & Mathies, R. A. Analysis of femtosecond dynamic absorption-spectra of nonstationary states. *Annu. Rev. Phys. Chem.* **43,** 497–523 (1992).

21. Rost, J. M., Schulz, K., Domke, M. & Kaindl, G. Resonance parameters of photo doubly excited helium. *J. Phys. B* **30,** 4663–4694 (1997).

22. Reinhardt, W. P. Complex coordinates in the theory of atomic and molecular-structure and dynamics. *Annu. Rev. Phys. Chem.* **33,** 223–255 (1982).

23. Paul, P. M. *et al.* Observation of a train of attosecond pulses from high harmonic generation. *Science* **292,** 1689–1692 (2001).

24. Kim, K. T. *et al.* Amplitude and phase reconstruction of electron wave packets for probing ultrafast photoionization dynamics. *Phys. Rev. Lett.* **108,** 093001 (2012).

25. Ullrich, J. *et al.* Recoil-ion and electron momentum spectroscopy: reaction-microscopes. *Rep. Prog. Phys.* **66,** 1463 (2003).

26. Morishita, T., Watanabe, S. & Lin, C. D. Attosecond light pulses for probing two-electron dynamics of helium in the time domain. *Phys. Rev. Lett.* **98,** 083003 (2007).

27. Palaudoux, J. *et al.* Multielectron spectroscopy: Auger decays of the krypton 3d hole. *Phys. Rev. A* **82,** 043419 (2010).

28. Augst, S., Meyerhofer, D. D., Strickland, D. & Chin, S. L. Laser ionization of noble-gases by Coulomb-barrier suppression. *J. Opt. Soc. Am. B* **8,** 858–867 (1991).

29. Assion, A. *et al.* Control of chemical reactions by feedback-optimized phase-shaped femtosecond laser pulses. *Science* **282,** 919–922 (1998).

Author Contributions C.O. and T.P. designed the experiment. C.O., A.K., P.R., R.H. and T.P. built the experimental apparatus. C.O., A.K., Y.Z., P.R. and T.P. conducted the experiments. C.O., A.K., S.H., R.H. and T.P. performed the experimental data analysis and interpretation, C.O., A.K., S.H., T.D., R.H. and T.P. carried out the few-level model simulation. L.A. designed and implemented the *ab initio* methods. L.A. and F.M. carried out the *ab initio* simulation and significantly contributed to the interpretation of the results. J.M. calculated the field-free wave functions. C.O., A.K., L.A., F.M. and T.P. wrote major parts of the manuscript. All authors contributed to the discussion of the results and commented on the manuscript.

Author Information Reprints and permissions information is available at www.nature.com/reprints. The authors declare no competing financial interests. Readers are welcome to comment on the online version of the paper. Correspondence and requests for materials related to the experiment and the few-level model should be addressed to T.P. (thomas.pfeifer@mpi-hd.mpg.de), and those related to the *ab initio* calculations should be addressed to F.M. (fernando.martin@uam.es).

METHODS

Experimental apparatus details. The laser system (commercial Femtolasers compact Pro Ti:Sapphire multipass amplifier; hollow-core fibre spectral broadening; temporal pulse compression with chirped mirrors) typically delivers sub-7 fs, ~730 nm, 0.3 mJ laser pulses at 4 kHz repetition rate. The carrier-envelope phase (CEP) was not stabilized but averaged over to avoid additional fluctuations from CEP noise in the high-harmonic spectrum, especially since our measurement scheme is insensitive to the CEP (see 'Effects of the attosecond pulse configuration and the CEP' below). The vacuum set-up is shown in Extended Data Fig. 1a. The laser pulses were focused (50 μm focal-spot size; peak intensities, 10^{14}–10^{15} W cm^{-2}) into a stainless-steel cell filled with neon gas, entering and exiting through 100 μm-diameter machine-drilled holes in the cladding. A small fraction of the visible (VIS) light was up-converted into the extreme ultraviolet (XUV) energy range, using high-harmonic generation (HHG) for attosecond pulse production[30]. The macroscopic parameters were optimized for continuous spectra (100 mbar neon backing pressure; cell position near the laser focus). In Extended Data Fig. 1b, a typical XUV spectrum is shown, alongside an XUV spectrum after transmission through a 100 mbar helium gas target. The co-propagating XUV and VIS pulses were separated by a 2 μm silicon nitride membrane with a ~2 mm-diameter centre hole, in combination with a concentrically mounted 200 nm aluminium filter behind the hole. This separation scheme makes use of the intrinsically lower divergence of the XUV beam. The time delay between the XUV and VIS pulses was obtained by a grazing-incidence (15°) split-mirror set-up consisting of an inner gold-coated mirror (2 mm size) for the XUV, and a surrounding silver mirror for the VIS. The inner mirror can be translated with respect to the outer mirror using a high-precision piezoelectric stage (~1 nm resolution; ~260 μm range). Both beams were refocused (1:1 geometry; 350 mm focal length) with a gold-coated toroidal mirror under the same 15° grazing angle of incidence into another stainless-steel cell filled with helium gas. The monolithic set-up guarantees a high interferometric stability (measured temporal precision, ~10 as), combined with broadband and high-throughput advantages of all-grazing-incidence optics. Spectral selection was achieved using thin metal filters (200 nm aluminium), transmitting in the 20–70 eV energy range[31]. The intensity of the VIS beam on the helium target was finely tuned using a picomotor-controlled iris diaphragm centred around both beams. The XUV radiation transmitted through the helium target was spectrally imaged using a flat-field spectrometer consisting of a variable-line-spacing (VLS) grating and a thermoelectrically cooled, back-illuminated XUV CCD camera. The VIS stray light was removed with a pair of 200 nm aluminium metal filters. The spectrometer calibration was obtained by identifying the observed $sp_{2,n+}$ two-electron resonance lines in helium and using tabulated experimental values of high-precision synchrotron measurements[15,32]. The spectral resolution ($\sigma = 20$ meV Gaussian standard deviation) near 60 eV resulted from a fit of the $2s2p$ resonance line. The target gas density (~100 mbar) was chosen such that the strongest $2s2p$ absorption line was still well below absorbance $A = 2$ to avoid dispersion and propagation effects[33]. The zero position of time delay was obtained by generating high harmonics in argon in the target gas cell, and accounting for the known thickness of the silicon nitride membrane and the aluminium filter.

Experimental data acquisition. Sets of XUV spectra were recorded as a function of time delay (from −18 to +34 fs in ~170 as steps; negative values correspond to VIS pulse arriving first) and VIS intensity (35 different iris diaphragm opening settings up to the 10^{12} W cm^{-2} peak-intensity regime), where the intensity calibration was obtained *in situ* as described below ('Intensity calibration'). Each single spectrum was obtained by integration over ~3,200 laser shots. For each VIS intensity, additional XUV spectra were recorded without the target helium gas to obtain reference spectra (Extended Data Fig. 1b). The absorbance A is obtained from the general formula $A = -\log_{10}(I_{SIG}/I_{REF})$, where I_{SIG} is the signal and I_{REF} is the reference spectral intensity. At an exemplary VIS intensity of 3.3×10^{12} W cm^{-2}, the two-dimensional absorbance, plotted versus time delay and photon energy, is displayed in Extended Data Fig. 1c. All relevant structures as discussed in the main text can already be seen. The noisy structures (horizontal lines) are a result of the non-simultaneous measurement of signal and reference XUV spectra, and were filtered out for our quantitative analysis using the following method. For each recorded signal XUV spectrum (containing absorption lines), a low-pass Fourier filter was used to filter out the 'slowly' modulating (~3.4 eV period) high-harmonic XUV spectrum. This *in situ* filtered spectrum $I_f(\omega)$ was scaled to obtain a reconstructed reference spectrum $I_{REF,rc}(\omega)$ using Beer's law: $I_{REF,rc}(\omega) = I_f(\omega)\exp[\sigma_{PCS}(\omega)l\rho]$, where σ_{PCS} is the known non-resonant photo-absorption cross-section of helium[34]. The path-length/density product $l\rho$ is the free scaling parameter and was determined to be $l\rho = (0.56 \pm 0.05) \times 10^{18}$ cm^{-2} via comparison with the measured spectral intensity I_{REF}. As a result of this reference-reconstruction method, the statistical noise of the two-dimensional absorbance plots is significantly reduced, as can be seen by comparing Extended Data Fig. 1c with Fig. 3a. The differential absorption spectra shown in Fig. 2 were generated by subtracting the field-free (no VIS laser interacting with the XUV-induced dipole at early delays) static spectra, plotting the change of the absorbance (ΔA).

Few-level model simulation. The model system consists of three autoionizing states, $2s2p$ ($^1\mathrm{P}^\mathrm{o}$), $2p^2$ ($^1\mathrm{S}^\mathrm{e}$) and $sp_{2,3+}$ ($^1\mathrm{P}^\mathrm{o}$), at excitation energies 60.15 eV, 62.06 eV and 63.66 eV, respectively, above the $1s^2$ ($^1\mathrm{S}^\mathrm{e}$) helium ground state[32,35]. These autoionizing states will be referred to as $|a\rangle$, $|b\rangle$ and $|c\rangle$, respectively, in the following. Other states belonging to the $N = 2$ doubly excited Rydberg series are off-resonance with respect to the coupling VIS laser (~1.7 eV photon energy) and/or are significantly lower in coupling strength, and are thus neglected. This subsystem of states is sufficient to reproduce the experimentally observed 1 fs quantum beat. The model is based on previous work[10,11] solving the time-dependent Schrödinger equation in the configuration basis of the VIS-coupled states. The parity-allowed ($^1\mathrm{S}^\mathrm{e} \leftrightarrow {}^1\mathrm{P}^\mathrm{o}$) transitions are expressed by the dipole matrix elements d_{nm} as depicted in Extended Data Fig. 2a, which also includes the configuration-interaction matrix elements $V_{\varepsilon,n}$ that connect the autoionizing states to their respective single-electron continua $|1s, \varepsilon s\rangle$ or $|1s, \varepsilon p\rangle$. In accordance with earlier approaches for a similar system[11], the non-resonant VIS-induced coupling of the $^1\mathrm{P}^\mathrm{o}$ states with the $|1s, \varepsilon s\rangle$ continuum is neglected. Also the VIS coupling between the two continua can be safely neglected in our intensity regime[10]. Extended Data Fig. 2b depicts the Schrödinger equation of the so-described few-level system, with the states' complex expansion coefficients $c_n(t)$, and using atomic units. The weak excitation with the broadband XUV field $F_{XUV}(t)$ is described in first-order perturbation theory, that is, $\partial_t c_g(t) = 0$, with $E_g = 0$. Under the rotating-wave approximation, $F_{XUV}(t)$ is taken as a complex quantity, neglecting the anti-resonant part of the interaction. The coupling between the excited bound states is mediated using the full time-dependent real representation of the VIS field $F_{VIS}(t)$. The continua are treated in the strong-field approximation as Volkov states with the vector potential $A_{VIS}(t) = -\int_{-\infty}^t dt' \, F_{VIS}(t')$ and are parameterized by their canonical momentum p. A one-dimensional treatment is justified owing to the linear polarization of the electric fields. The continuum states are described as quasi-discrete non-interacting states separated in momentum by Δp. To suppress continuum revivals that are an artefact of this discretization, a constant decay rate γ is employed which spectrally broadens the quasi-discrete states to a mutual overlap. The configuration-interaction matrix elements $V_{\varepsilon,n} = \langle 1s, \varepsilon|\boldsymbol{H}|n\rangle \equiv V_n$, which describe autoionization, are taken to be constant (that is, energy independent) in the vicinity of each configuration state, in accordance with Fano's original theory[17].

Direct numerical integration of the time-dependent complex expansion coefficients $c_n(t)$ was performed with a split-step-like approach, where, for each time interval Δt, different subsystems were evaluated separately. The corresponding five steps were as follows. (i) The perturbative excitation of states $|a\rangle$, $|c\rangle$ and the set of $|1s, \varepsilon p\rangle$ continuum states in the XUV laser field. (ii) The coupling of the three bound states $|a\rangle$, $|b\rangle$ and $|c\rangle$ in the VIS laser field. (iii) The coupling of the three bound states $|n\rangle$ with their corresponding continuum states $|1s, \varepsilon p\rangle$ and $|1s, \varepsilon s\rangle$ owing to configuration interaction. (iv) The field-free evolution of the three bound states with eigenenergies E_n. (v) The VIS-laser-dressed evolution of the quasi-discrete continuum states. For each of these five steps, the corresponding subsystem was diagonalized, and temporal evolution thus corresponds to the multiplication of a complex phase factor 'exp($-i\lambda_j\Delta t$)', with λ_j being the eigenvalues of the diagonalized subsystem after a unitary transformation. For each time point, the time-dependent dipole moment $D(t) = d_{ga}c_a(t) + d_{gc}c_c(t) + d_g\sum_\varepsilon c_{\varepsilon p}(t)$ between the ground state $|g\rangle$ and the dipole-allowed $|a\rangle$ and $|c\rangle$ states as well as the $|1s, \varepsilon p\rangle$ continuum states was evaluated, where the ground–continuum dipole matrix element $d_g \equiv d_{g\varepsilon}$ was assumed to be independent of energy. The absorption spectra were calculated[20] via the Fourier transform of $D(t)$, which is proportional to the polarization $P(\omega)$ of the system. Dividing this quantity by the XUV laser spectrum $F(\omega)$ (to obtain a quantity that, in the absence of the VIS field, is proportional to the susceptibility $\chi(\omega)$ of helium, where $P(\omega) = \varepsilon_0\chi(\omega)F(\omega)$; in the presence of the VIS field this corresponds to a generalized linear susceptibility as discussed in ref. 20) and taking the imaginary part of this ratio leads to the XUV absorption profile. This quantity is proportional to the experimentally reconstructed absorbance introduced in 'Experimental data acquisition' in our limit of low absorption and, thus, negligible propagation and dispersion effects.

The numerical parameters used (in the respective atomic units) were the discretization time step $\Delta t = 1$ a.u. (0.0242 fs); the total simulation time $T = 32,000$ a.u. (774 fs); the discretized single-electron continuum momentum, which ranged from $p_{min} = \pm 1.35$ a.u. (that is, $E_{min} = 24.8$ eV) to $p_{max} = \pm 2.80$ a.u. (that is, $E_{max} = 106.7$ eV) in 100 steps with $\Delta p = \pm 0.0145$ a.u. (that is, in total 400 quasi-discrete continuum states) and decay rate $\gamma = 0.1$ a.u.; the energies, widths and asymmetry parameters of the $^1\mathrm{P}^\mathrm{o}$ states[15,32] $E_a = 60.147$ eV, $\Gamma_a = 37$ meV and $q_a = -2.75$, and $E_c = 63.658$ eV, $\Gamma_c = 10$ meV and $q_c = -2.53$; the energy and width of the $^1\mathrm{S}^\mathrm{e}$ state[35,36] $E_b = 62.06$ eV and $\Gamma_b = 6$ meV; and the dipole matrix element $d_{ab} = 2.17$ a.u., which was taken from ref. 8, whereas $d_{bc} = -0.81$ a.u. was calculated (E. Lindroth, personal communication, 2011). The remaining V_n, d_{gn} and d_g were determined for the simulated absorption spectra to match known experimental and theoretical line shapes with above printed values. The laser pulses were defined as $F^{(0)}\exp[-(t/t_G)^2]\cos(\omega_c t + \varphi_{CEP})$,

with peak electric field strength $F^{(0)}$; Gaussian pulse duration $t_G = t_p/\sqrt{[2\ln(2)]}$, where t_p denotes the full-width at half-maximum intensity; the centre frequency ω_C; and the carrier-envelope phase (CEP) φ_{CEP}. The time discretization and total time simulated allowed us to correctly describe all dynamics in a reasonable amount of computation time (the narrowest linewidth of $\Gamma_b = 6$ meV corresponds to a $\sim$110 fs lifetime). The decay rate γ effectively maintains the autoionized electrons for $\sim$16 a.u., which is a reasonable upper estimate for the spatial extent of the localized two-electron states.

The simulation was validated by using a quasi-monochromatic ($t_G \gg T$) VIS laser field ($\lambda \approx 730$ nm) of increasing field strength $F^{(0)}_{VIS}$, where the obtained cycle-averaged absorbance is depicted in Extended Data Fig. 2c. As expected, line splitting and a.c. Stark shifts according to the Rabi frequency $d_{nm}F^{(0)}_{VIS}$ occur owing to Rabi cycling among the three states. To approach the situation realized in the experiments, the temporal evolution of their coefficients is shown in Extended Data Fig. 2d–f at various time delays, where a 7 fs VIS laser pulse was applied instead of the quasi-monochromatic laser field. Significant rearrangement of population between the states occurs, and is maintained after the VIS pulse interaction. This intuitively illustrates how the VIS laser pulse affects the relative population of the two-electron states, which is experimentally accessible in the measured absorption line shapes because these are derived from the oscillating dipole moment $D(t)$. The few-level model simulation was used in the reconstruction of the experimentally observed two-electron wave packet, which allowed for an independent comparison with the full *ab initio* 3D TDSE calculation, and to check for possible effects of various different pulse configurations on the investigated dynamics.

Ab initio TDSE simulation. The *ab initio* transient absorption spectrum was reproduced using the velocity-gauge perturbative expression

$$\sigma_{TAS}(\omega) = \frac{4\pi}{\omega} \mathrm{Im}\, \frac{\tilde{p}(\omega)}{\tilde{A}(\omega)} \qquad (1)$$

where ω is the field angular frequency, $\tilde{p}$ is the Fourier transform of the total electronic canonical momentum expectation value

$$\tilde{p}(\omega) = \frac{1}{\sqrt{2\pi}} \int_{-\infty}^{\infty} dt\, e^{-i\omega t} p(t)$$

$$p(t) = \langle \psi(t) | p_z | \psi(t) \rangle$$

$\tilde{A}$ is the Fourier transform of the XUV vector potential amplitude, and $\psi(t)$ is the wavefunction for the helium atom in the presence of the external field. The use of equation (1) is justified in the limit of optically thin samples. Already for VIS pulse intensities of the order of few TW cm^{-2}, the optical response $p(t)$ depends non-perturbatively on the VIS external field. For this reason, $p(t)$ was obtained by integrating the TDSE

$$i\partial_t \psi(t) = \lfloor H_0 + V_{abs} + \alpha \vec{A}(t)\cdot\vec{p} \rfloor \psi(t)$$

where H_0 is the field-free electrostatic Hamiltonian of helium, $\alpha\vec{A}(t)\cdot\vec{p}$ is the minimal-coupling term that accounts for the interaction of the atom with the external field, and V_{abs} is a symmetric complex local potential that prevents reflection from the boundary of the quantization box where the wavefunction is defined. To solve the TDSE accurately, the wavefunction was expanded on the eigenstates of H_0, projected on a two-particle B-spline close-coupling basis with pseudostates[37,38]. In such a basis, the angular part is represented by bipolar spherical harmonics and the radial part by B-splines with an asymptotic knot spacing of 0.5 a.u. Each total angular momentum comprises all the partial-wave channels with configurations of the form $Nl\varepsilon_{l'}$ with $N \leq 2$, and a full-CI localized channel $nln'l'$ that reproduces short-range correlations between the two electrons. In the presence of the field, the TDSE was integrated numerically with a second-order midpoint exponential time-step propagator[19],

$$\psi(t+dt) = e^{-iV_{abs}} e^{-iH_0 dt/2} e^{-idt\alpha\vec{A}(t+dt/2)\cdot\vec{p}} e^{-iH_0 dt/2} \psi(t)$$

The action of the second exponential, which depends on the external fields and couples blocks with different symmetry, is evaluated with an iterative Krylov-space method. In the simulation, we included states with total angular momentum up to $L_{max} = 10$ and, for the localized channel, orbital angular momentum up to $l_{max} = 5$. We ascertained the convergence of the theoretical results with respect to the most relevant expansion parameters in the state representation by conducting additional representative simulations with either $L_{max} = 15$ or $l_{max} = 10$, as well as by including the $N = 3$ partial-wave channels in the close-coupling expansion. After the external field has vanished, the Hamiltonian no longer depends on time and the propagation becomes trivial:

$$\psi(t) = \sum_i |\varphi_{R,i}\rangle e^{-iE_i(t-t')} \langle \varphi_{L,i} | \psi(t') \rangle$$

Here the states $\varphi_{L/R}$ are the left and right eigenstates of the quenched Hamiltonian $H_Q = H_0 + V_{abs}$, whose complex eigenvalues E_i have non-positive imaginary components:

$$H_Q = \sum_i |\varphi_{R,i}\rangle E_i \langle \varphi_{L,i} |$$

$$\langle \varphi_{L,i} | \varphi_{R,j} \rangle = \delta_{ij}$$

$$\mathrm{Im}\, E_i \leq 0 \;\; \forall i$$

The expectation value $p(t)$ can conveniently be split into two smooth components

$$p(t) = p^-(t) + p^+(t)$$

defined in such a way that $p^-(t)$ becomes negligible shortly after the external field has vanished, whereas $p^+(t)$ is zero before and while the external field is non-zero. As a result of the separation, the Fourier transform of $p(t)$ also splits into the sum of two terms

$$\tilde{p}(\omega) = \tilde{p}^-(\omega) + \tilde{p}^+(\omega)$$

The first Fourier transform was evaluated numerically from tabulated values of $p(t)$ on a dense time grid. The second Fourier transform was instead evaluated analytically from the spectral resolution of the quenched Hamiltonian, the dipole transition matrix elements from the ground state, and the expansion coefficients of the wavefunction at a given time after the external fields have vanished on the numerical basis used to conduct the time propagation. This way of proceeding provides the same result as an infinite time propagation. To compare with the wave packets reconstructed from the experiment, the spatial part of the theoretical wave function $\psi(z_1, z_2; t)$ was tabulated as a function of the Cartesian coordinates z_1 and z_2 when both the electrons are aligned to the field polarization axis, for selected pump−probe time delays and observation times.

Intensity calibration. The simulated few-level dynamics, which is in good qualitative and quantitative agreement with the experimental data and is thus well understood, was used to assess the intensity of the VIS pulse in the interaction region. Both for the numerical and for the experimental results, small temporal regions (averaged over two modulation periods) around 0 fs and around $\sim$5 fs time delay (where the Autler–Townes splitting of the $2s2p$–$2p^2$ doublet is strongest; for the numerical results this was $\sim$3 fs) were averaged and the spectra were plotted as a function of the VIS intensity (in the simulation; Extended Data Fig. 3a) and iris diaphragm openings (in the experiment; Extended Data Fig. 3b). By quantifying the induced a.c. Stark shifts of the light-induced $2s2p$–$2p^2$ Autler–Townes doublet in the experiment, and comparing these shifts with the simulated data (based on the known and experimentally confirmed[8] dipole matrix element between the two states) an *in situ* intensity calibration was achieved, shown in Extended Data Fig. 3c. The calibration includes an average over various VIS pulse durations (ranging from 5 to 30 fs) to account for the effect of a >7 fs pedestal in the VIS pulse, which is typical of the hollow-fibre/chirped-mirror pulse compression method employed.

Effects of the attosecond pulse configuration and the CEP. The experimental data were obtained by averaging over the CEP. In addition, the coherent XUV excitation spectrum consisted of a train of few attosecond pulses, which is indicated by energy modulations on top of the broad XUV spectra as shown in Extended Data Fig. 1b. Both these effects are negligible for the purposes of observing the discussed effects, as will be shown in the following. Three different XUV pulse configurations have been simulated and are plotted in Extended Data Fig. 4a, and show no significant changes in the absorbance spectra. This is a direct consequence of the well-known[23] phase locking of the attosecond pulses to the half-cycles of the generating intense VIS pulses. In the energy domain, this corresponds to a well-defined coherent excitation spectrum over a broadband spectral range. The insensitivity to the XUV pulse configuration was also confirmed experimentally by performing measurements with and without CEP stabilization. By comparing the corresponding plots in Extended Data Fig. 4b, we see that the additional CEP stabilization in the experiment does not modify the results obtained in the absence of CEP stabilization. Thus, to avoid any sources of error from an imperfect absolute CEP determination (because such a determination does not at present exist for transient-absorption measurements), CEP temporal drift correction, spatial effects such as potential inhomogeneity across the beam profile, or Gouy phase slips in the exact experimental interaction region (extended He target cell), we measured the bulk of our data in the well-reproducible situation of non-stable (and, thus, fully statistical) CEP. We also confirmed the insensitivity of the measurement to the exact pulse-train configuration in the weak-field VIS interaction case for which we extracted the wave-packet phase information shown

in Fig. 2. The results for single-, double- and multi-attosecond-pulse excitation situations are shown in Extended Data Fig. 5. To define the attosecond pulse and its time of arrival with respect to the (generating) VIS laser pulse, we used the coherence (phase locking) between two harmonics, which has been confirmed numerous times to be present in high-harmonic generation since its first direct measurement via interferometric two-photon photoelectron spectroscopy[23]. Assuming this phase locking of two harmonics in the energy region 60–64 eV produced the attosecond pulse trains in the model simulation, and also defined the individual attosecond pulse duration to be ~600 as.

Measuring the wave-packet phase in real/elapsed time. In the experiment, we measured changes of the spectrally resolved absorbance (ΔA), as a function of time delay τ between an attosecond-pulsed XUV excitation and a VIS coupling pulse. For the case of weak VIS intensity, the coupling process can be considered a weak-field probe process, which does not significantly affect the phases nor the population of the quantum states $2s2p$ and $sp_{2,3+}$ contributing to the wave packet:

$$|\Psi(t)\rangle \propto \exp\left(-\frac{\Gamma_{2s2p}}{2}t\right)|2s2p\rangle + a\ \exp[-i\varphi(t)]\exp\left(-\frac{\Gamma_{sp2,3+}}{2}t\right)|sp_{2,3+}\rangle$$

In the simulations shown in Extended Data Fig. 5, conducted at the same intensity as for the experimental results in Fig. 2a, we confirmed that population transfer to the near-resonant $2p^2$ state was below 10%. In that weak-field case, the measured ΔA–τ data can be converted into information on the wave-packet states' relative-phase evolution $\varphi(t)$ in real time t (elapsed time after excitation). To define elapsed/real time zero, we used the arrival time of the exciting attosecond pulse, or the most intense central attosecond pulse in the case of a short pulse train, as depicted in Extended Data Fig. 5. A lineout of ΔA versus τ at a spectral position near the $sp_{2,3+}$ resonance at 63.67 eV (where ΔA shows pronounced changes with τ) is shown in Extended Data Fig. 6a and used to map $\Delta A(\tau)$ to $\varphi(t)$. The oscillation of $\Delta A(\tau)$ is almost fully independent of whether the excitation occurs with isolated attosecond pulses or with pulse trains of two or several attosecond pulses. The wave-packet phase $\varphi(t)$, defined as the time-dependent phase difference between the $2s2p$ and $sp_{2,3+}$ state coefficients, was read out from the simulation for all pulse configurations and compared with the phase $\varphi_A(\tau)$ of the oscillation with $\Delta A(\tau) \propto \cos[\varphi_A(\tau)] + \text{const}$ for $t = \tau$, as shown in Extended Data Fig. 6b. The phase $\varphi_A(\tau)$ was retrieved via Fourier analysis, taking the full modulation bandwidth into account as shown in Extended Data Fig. 5g, h. The phases of the wave packet, as excited by the different pulse configurations, are in excellent agreement, again showing that the wave packet is well defined even in the absence of isolated attosecond pulses or CEP locking. The difference between $\varphi_A(\tau)$ (measurable quantity) and $\varphi(t)$ (the relative phase between the quantum states defining the wave packet) was extracted and is shown in Extended Data Fig. 6c. This phase difference is almost independent of the XUV excitation configuration (isolated attosecond pulses versus trains of attosecond pulses), and was thus used in the experiment to retrieve the wave-packet phase as a function of elapsed time t from the measured $\Delta A(\tau)$ data. The experimental result is shown in Fig. 2d, e, where the error bar on the experimental wave-packet phase reconstruction as shown there includes the small error given by the experimental uncertainty in the exact attosecond pulse-train configuration, as discussed here. In Extended Data Fig. 6d, we also show that the amplitude ratio a of the wave packet remains well defined (within 10% amplitude-ratio fluctuations) despite the differences in the XUV excitation configurations. Fluctuations of the order of 10% in the high-harmonic spectra are typically present also in CEP-stabilized laser systems driving HHG, either by CEP noise or shot-to-shot driver-pulse intensity noise.

Line-shape analysis for phase retrieval. As was demonstrated in ref. 13, the Fano q asymmetry parameter can be directly related to a phase shift φ of the temporal dipole response after δ-like excitation via

$$\varphi = 2\arg(q - i) \tag{2}$$

This phase shift can be controlled using a short-pulsed laser field as described in the main text in connection to Fig. 4. The laser-controlled phase manipulation of

the states right after excitation can thus be read out by fitting a Fano line shape to the measured absorption spectrum. The absorption line shape obtained from the *ab initio* simulation (shown in Fig. 4b), is directly fitted with an asymmetric Fano line profile, using

$$S_{FANO} = \frac{a}{q^2+1}\left[\frac{(q+\varepsilon)^2}{1+\varepsilon^2} - 1\right] + b \tag{3}$$

$$\varepsilon = \frac{E - E_r}{\Gamma/2}$$

where ε is the reduced energy. Here all parameters such as the strength a, the offset b, the asymmetry parameter q, the resonance position E_r and the decay width Γ converged to a least-squares minimum. Both the fitted intensity-dependent amplitude $a(I)$ and the phase $\varphi(I)$, where the latter was obtained from q after using equation (2), perfectly agree with the states' complex expansion coefficients. This is shown for the intensity-dependent phase $\varphi(I)$ of the $2s2p$ and $sp_{2,3+}$ states in Fig. 4e, f. Extended Data Fig. 7c, d shows the related fitted line shapes for several VIS laser intensities in the energy region where the least-squares fit was performed, which is 60.11–60.21 eV for the $2s2p$ state and 63.56–63.76 eV for the $sp_{2,3+}$ state. In fitting the experimentally recorded line shapes, we took into account the finite spectrometer resolution, which is of the order of the decay width of the states. Because the XUV intensity $I_{SIG}(E)$ was measured after transmission through the helium target, $10^{-S_{FANO}}$ needed to be convolved with the spectrometer response function, which excluded the formulation of an analytical fit function. Formally, the experimentally observed line shape is parameterized via

$$S_{FANO,EXP} = -\text{Log}_{10}\left[\left(10^{-S_{FANO}}\right) \otimes \frac{1}{\sqrt{2\pi}\sigma}\exp\left[-\frac{E^2}{2\sigma^2}\right]\right]$$

where $\otimes$ denotes the convolution, S_{FANO} is given in equation (3) and $\sigma = 0.020$ eV is the experimentally determined detector resolution. In the presence of experimental noise and a limited number of data points, both E_r and Γ were kept constant for all VIS laser intensities using literature values. $S_{FANO,EXP}$ was numerically computed in the parameter space spanned by q, a and b, and the error sum of mean squared $S_{FANO,EXP}$ values with respect to the experimental data points was minimized within the same energy region as above. The results are shown in Extended Data Fig. 7a, b and confirm the convergence of the numerically performed minimization procedure. The intensity-dependent phase $\varphi(I)$, extracted from Fano line-shape analysis, is shown in Fig. 4c, d. The error bars were determined by fitting three equivalent experimental data sets and computing the standard deviation.
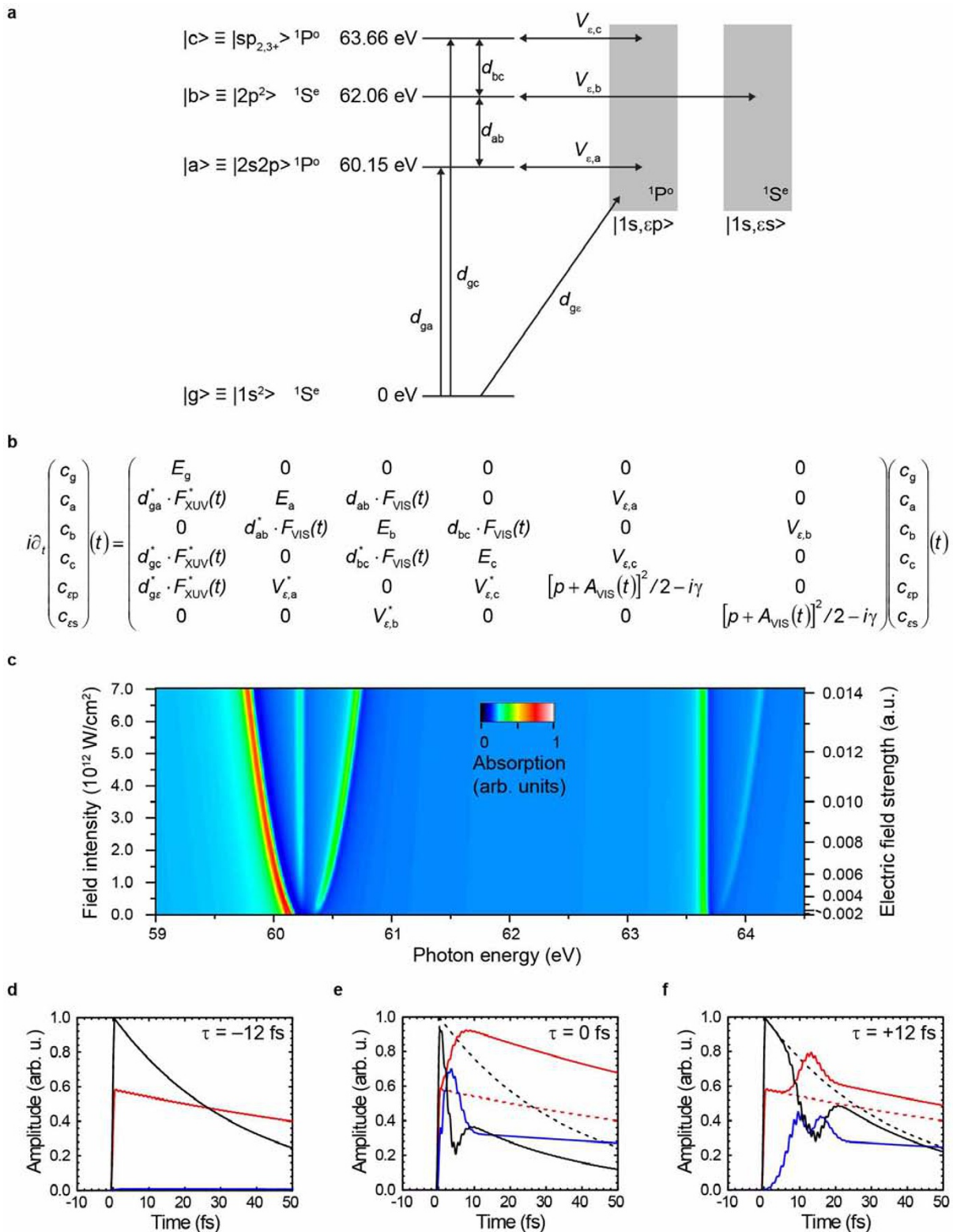
30. Krausz, F. & Ivanov, M. Attosecond physics. *Rev. Mod. Phys.* **81,** 163–234 (2009).
31. Henke, B., Gullikson, E. & Davis, J. X-ray interactions: photoabsorption, scattering, transmission, and reflection at E = 50–30,000 eV, Z = 1–92. *At. Data Nucl. Data Tabl.* **54,** 181–342 (1993).
32. Domke, M., Schulz, K., Remmers, G., Kaindl, G. & Wintgen, D. High-resolution study of $^1P^o$ double-excitation states in helium. *Phys. Rev. A* **53,** 1424–1438 (1996).
33. Santra, R., Yakovlev, V. S., Pfeifer, T. & Loh, Z.-H. Theory of attosecond transient absorption spectroscopy of strong-field-generated ions. *Phys. Rev. A* **83,** 033405 (2011).
34. Samson, J. A. R., He, Z. X., Yin, L. & Haddad, G. N. Precision measurements of the absolute photoionization cross-sections of He. *J. Phys. B* **27,** 887 (1994).
35. Hicks, P. J. & Comer, J. Ejected electron spectroscopy of autoionizing states excited by low energy electron impact. *J. Phys. B* **8,** 1866 (1975).
36. Bürgers, A., Wintgen, D. & Rost, J.-M. Highly doubly excited S states of the helium atom. *J. Phys. B* **28,** 3163–3183 (1995).
37. Argenti, L. & Moccia, R. K-matrix method with B-splines: sigma (nl), beta(n) and resonances in He photoionization below N=4 threshold. *J. Phys. B* **39,** 2773–2790 (2006).
38. Argenti, L. & Moccia, R. Helium 2(3)S photoionization up to the N=5 threshold. *J. Phys. B* **41,** 035002 (2008).
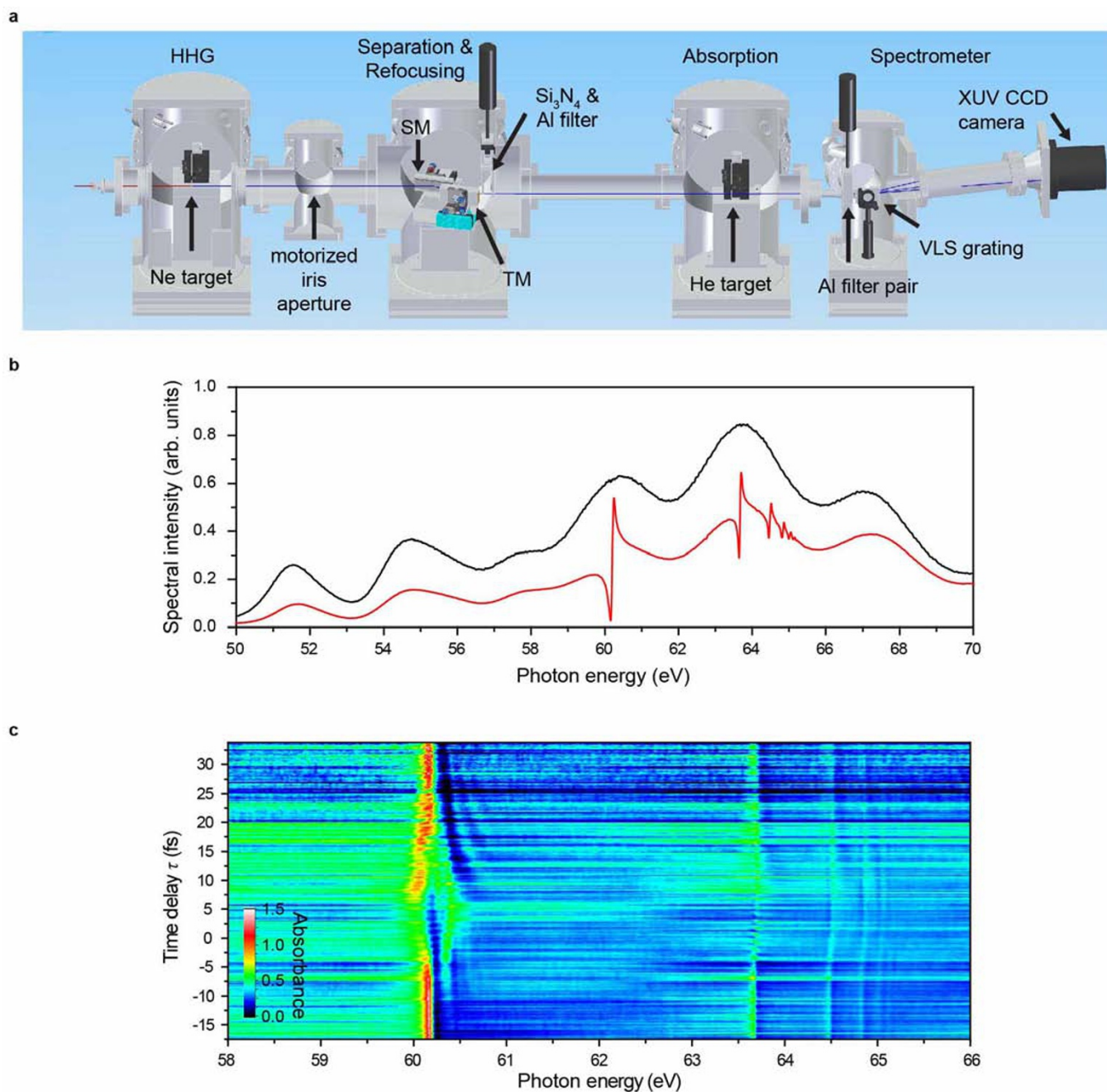
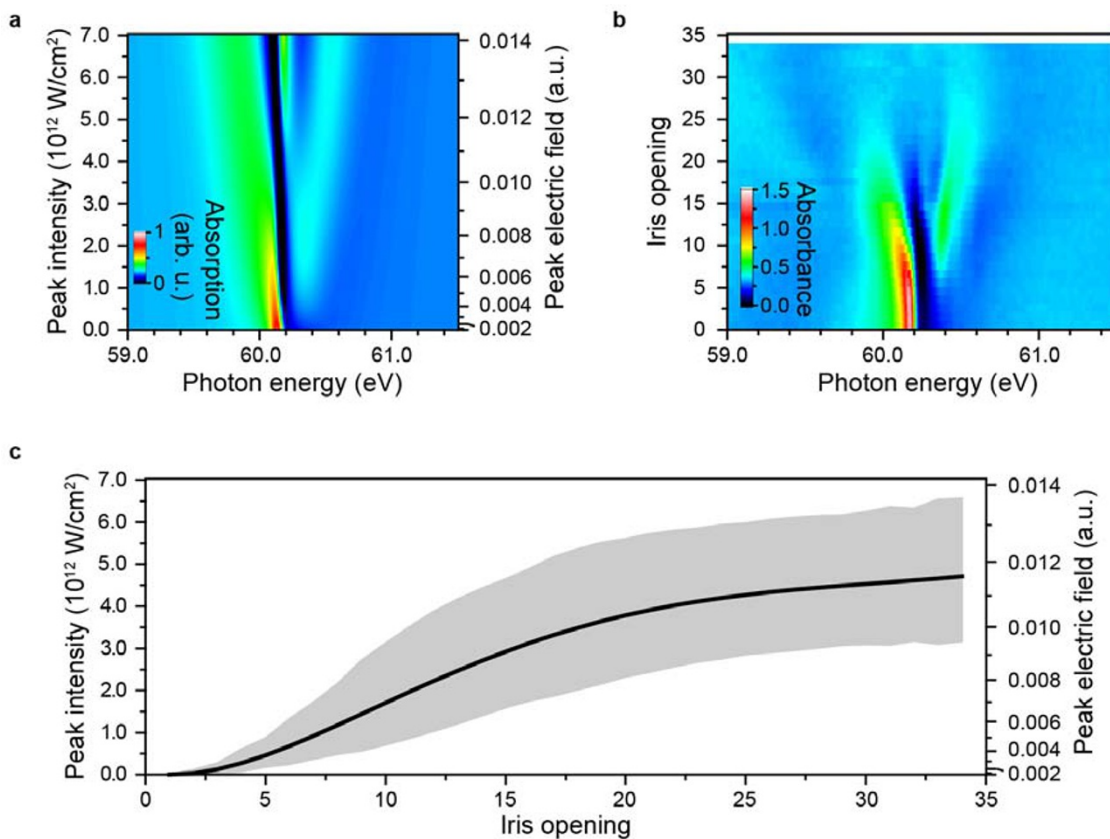**Extended Data Figure 1 | Experimental apparatus and recorded data.**
a, Design view of the experimental set-up, consisting of a neon (Ne) gas target for high-harmonic generation (HHG), a motorized iris aperture, a split mirror (SM) in combination with a thin silicon nitride (Si_3N_4) membrane and an aluminium (Al) filter, a focusing toroidal mirror (TM), a dense ($\sim$100 mbar) absorbing helium (He) target, and a home-built high-resolution spectrometer, which consists of a variable-line-spacing (VLS) grating, a cooled ($-50\,^\circ C$) XUV CCD camera, and a pair of Al filters for stray-light suppression. **b**, Recorded XUV reference spectrum (black line; no He gas in target cell) in the 50–70 eV energy range, averaged over $\sim$64,000 laser shots, and recorded XUV signal spectrum after transmission through the dense He gas target (red line), averaged over $\sim$640,000 laser shots. The statistical error is of the order of the line thickness. **c**, Two-dimensional absorbance at a calibrated VIS peak intensity of $3.3 \times 10^{12}\,W\,cm^{-2}$. The plot consist of 300 single absorbance spectra (for details and definition, see 'Experimental data acquisition' in Methods), that were obtained with a time-delay step size of $\sim$170 as.

a

$|c\rangle \equiv |sp_{2,3+}\rangle$ ${}^1\mathrm{P}^o$ 63.66 eV

$|b\rangle \equiv |2p^2\rangle$ ${}^1\mathrm{S}^e$ 62.06 eV

$|a\rangle \equiv |2s2p\rangle$ ${}^1\mathrm{P}^o$ 60.15 eV

$V_{\varepsilon,c}$
$V_{\varepsilon,b}$
$V_{\varepsilon,a}$

d_{bc}
d_{ab}

${}^1\mathrm{P}^o$ ${}^1\mathrm{S}^e$
$|1s,\varepsilon p\rangle$ $|1s,\varepsilon s\rangle$

d_{gc}
$d_{g\varepsilon}$
d_{ga}

$|g\rangle \equiv |1s^2\rangle$ ${}^1\mathrm{S}^e$ 0 eV

b

$$i\partial_t \begin{pmatrix} c_g \\ c_a \\ c_b \\ c_c \\ c_{\varepsilon p} \\ c_{\varepsilon s} \end{pmatrix}(t) = \begin{pmatrix} E_g & 0 & 0 & 0 & 0 & 0 \\ d_{ga}^* \cdot F_{XUV}^*(t) & E_a & d_{ab} \cdot F_{VIS}(t) & 0 & V_{\varepsilon,a} & 0 \\ 0 & d_{ab}^* \cdot F_{VIS}(t) & E_b & d_{bc} \cdot F_{VIS}(t) & 0 & V_{\varepsilon,b} \\ d_{gc}^* \cdot F_{XUV}^*(t) & 0 & d_{bc}^* \cdot F_{VIS}(t) & E_c & V_{\varepsilon,c} & 0 \\ d_{g\varepsilon}^* \cdot F_{XUV}^*(t) & V_{\varepsilon,a}^* & 0 & V_{\varepsilon,c}^* & [p + A_{VIS}(t)]^2/2 - i\gamma & 0 \\ 0 & 0 & V_{\varepsilon,b}^* & 0 & 0 & [p + A_{VIS}(t)]^2/2 - i\gamma \end{pmatrix} \begin{pmatrix} c_g \\ c_a \\ c_b \\ c_c \\ c_{\varepsilon p} \\ c_{\varepsilon s} \end{pmatrix}(t)$$

c

d $\tau = -12$ fs

e $\tau = 0$ fs

f $\tau = +12$ fs

Extended Data Figure 2 | Few-level model simulation details. a, Level scheme of the simulated subsystem, including the ground state $|g\rangle \equiv |1s^2\rangle$, the autoionizing bound states $|a\rangle \equiv |2s2p\rangle$, $|b\rangle \equiv |2p^2\rangle$ and $|c\rangle \equiv |sp_{2,3+}\rangle$, and the continua $|1s,\varepsilon p\rangle$ and $|1s,\varepsilon s\rangle$, all coupled via the dipole matrix elements d_{nm} as depicted. The configuration-interaction matrix elements $V_{\varepsilon,n}$ couple the excited states with their corresponding (symmetry ${}^1\mathrm{P}^o$ or ${}^1\mathrm{S}^e$) continua. **b**, Schrödinger equation describing the temporal evolution of the coupled states' expansion coefficients $c_n(t)$, resulting from the respective coupling pathways depicted in **a**. Further explanations and definitions of parameters are given in 'Few-level model simulation' in Methods. **c**, Simulated

two-dimensional absorbance plot of the few-level system assuming a quasi-monochromatic VIS field of 730 nm wavelength. The absorbance spectra were temporally averaged over one VIS laser cycle (XUV/VIS delay), and convolved with the experimental detector resolution ($\sigma = 20$ meV). **d–f**, Simulated temporal evolution of $|c_n(t)|$ of the three autoionizing states $2s2p$ (${}^1\mathrm{P}^o$; black lines), $2p^2$ (${}^1\mathrm{S}^e$; blue lines) and $sp_{2,3+}$ (${}^1\mathrm{P}^o$; red lines) where the ${}^1\mathrm{P}^o$-symmetry states were weakly populated by an XUV attosecond pulse at time $t = 0$ fs. All states were coupled by a VIS pulse (7 fs, 730 nm, 3×10^{12} W cm^{-2}) at three different time delays τ. The dashed curves show the states' evolution in the absence of the VIS field.

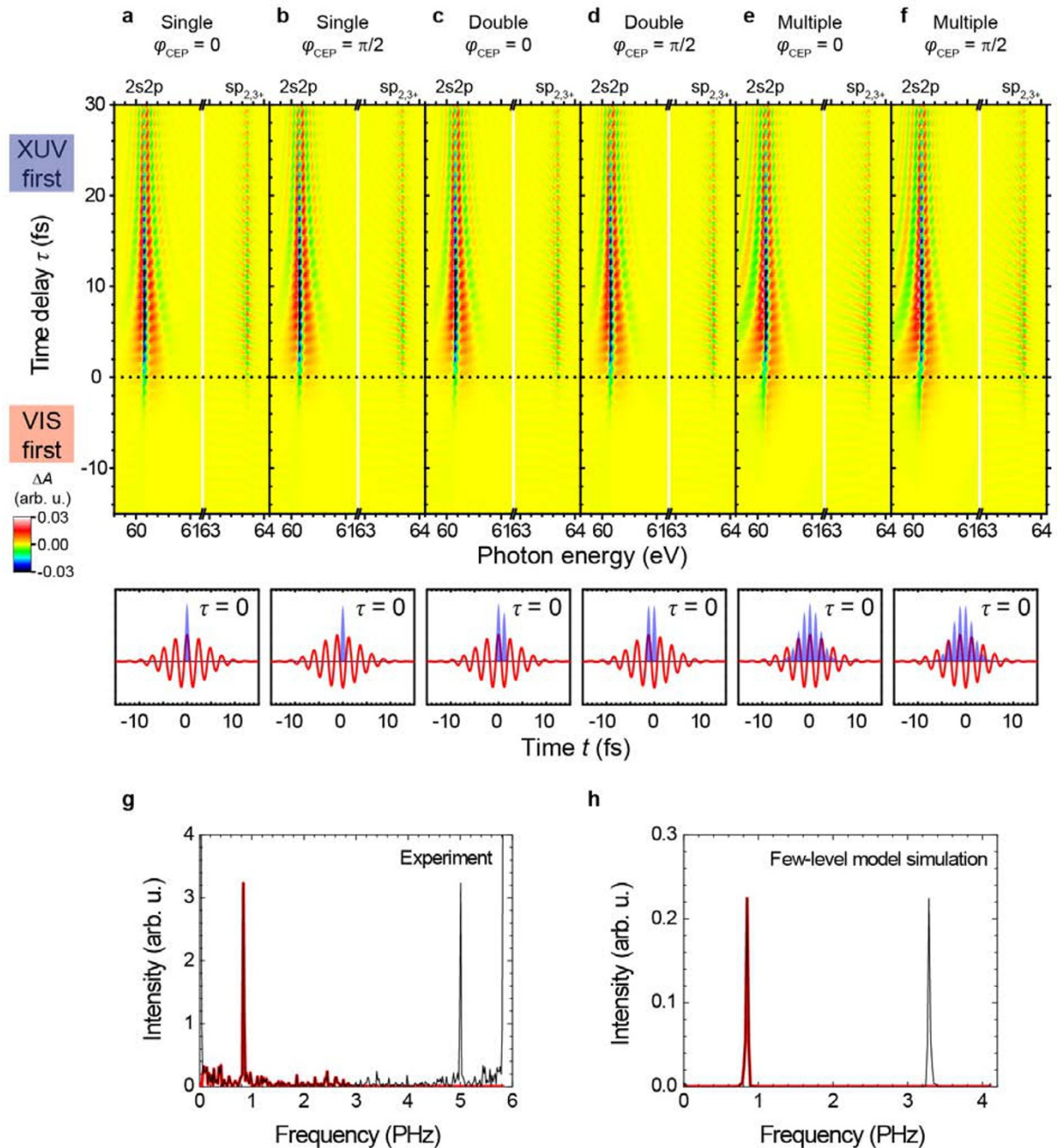**Extended Data Figure 3 | Intensity calibration of the experimental data.**
a, Calculated absorbance for a 7 fs, ~730 nm VIS laser pulse at increasing intensity. **b**, Experimentally measured absorbance for increasing openings of the iris diaphragm. For **a** and **b**, the time delay was set to where the Autler–Townes splitting is at maximum, averaged over two modulation periods. **c**, The comparison of maximum absorbance of the left-shifting $2s2p$ line (starting from 60.15 eV) between numerical and experimental results yields an *in situ* mapping between the VIS intensity and the iris opening in the experiment (black line). The grey shaded area denotes the standard deviation, taking into account different VIS durations and an additional comparison near 0 fs time delay, and thus represents the systematic uncertainty of the monotonically increasing intensity-calibration curve.
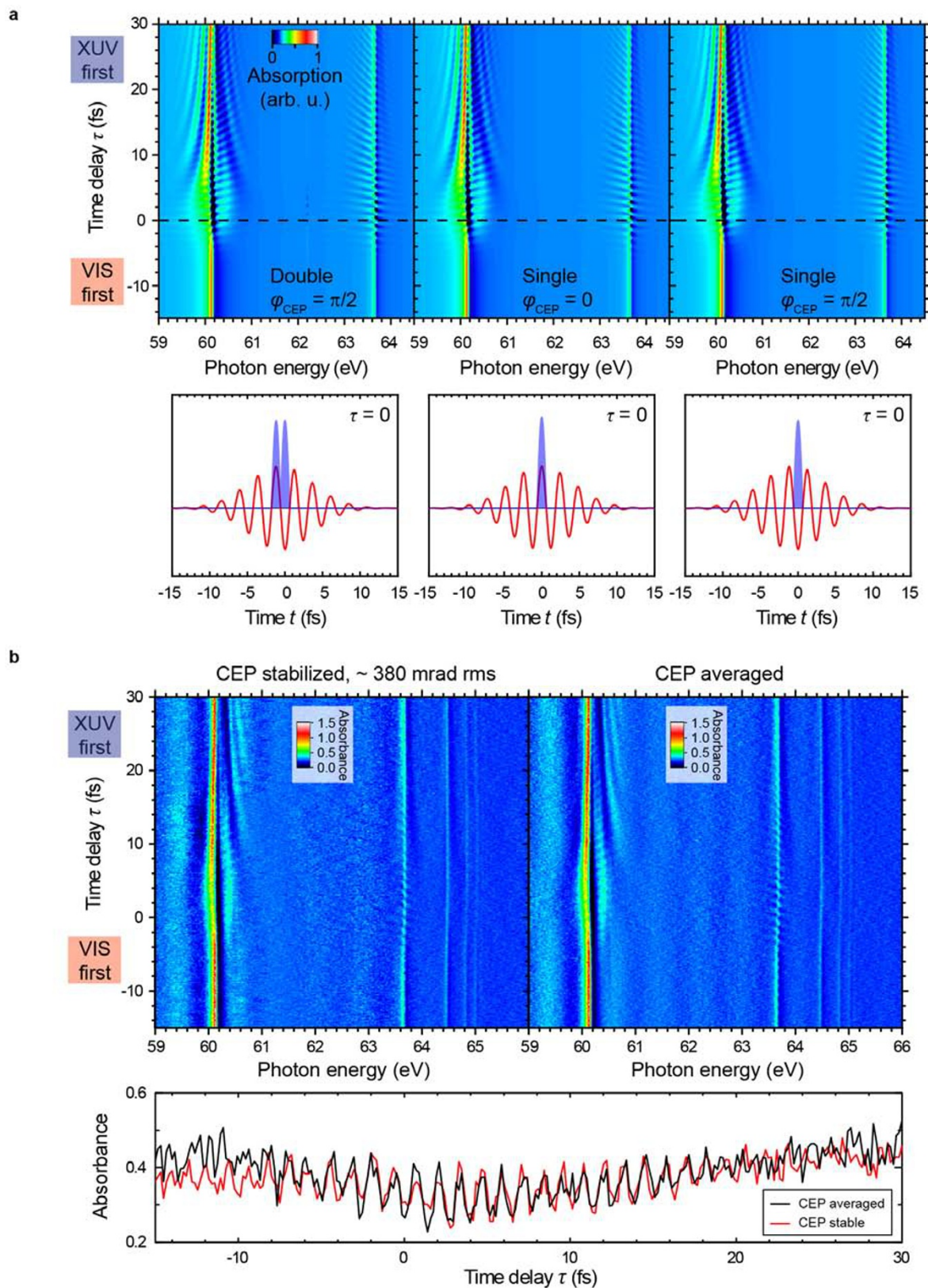
Extended Data Figure 4 | Effects of the attosecond pulse configuration and the carrier envelope phase. a, Simulated absorbance plots (top) for different XUV pulse configurations: two attosecond pulses, $\varphi_{CEP} = \pi/2$ (left); one attosecond pulse, $\varphi_{CEP} = 0$ (middle); one attosecond pulse, $\varphi_{CEP} = \pi/2$ (right). The VIS pulse duration was 7 fs with 3×10^{12} W cm^{-2} peak intensity, where the respective XUV/VIS pulse configurations are illustrated at zero time delay (bottom). **b,** Experimentally measured absorbance plots for CEP stabilization (top left; with root mean squared residual statistical noise of 0.38 rad) and CEP non-stabilization (top right). The observed time-dependent features, including the lineout at photon energy 63.66 eV (bottom) are practically identical for the CEP-stabilized and the non-CEP-stabilized measurements. Any significant temporal jitter between the attosecond pulses and the VIS carrier wave in the HHG process, for the case of statistical CEP, would correspond approximately to an averaging over a range of time delays for the case of a CEP-stable measurement, smearing out subcycle oscillations in the absorbance. This is clearly not observed.

Extended Data Figure 5 | Simulated absorbance changes (ΔA) for low VIS intensity and different pulse configurations. **a**, One attosecond pulse, $\varphi_{CEP} = 0$. **b**, One attosecond pulse, $\varphi_{CEP} = \pi/2$. **c**, Two attosecond pulses, $\varphi_{CEP} = 0$. **d**, Two attosecond pulses, $\varphi_{CEP} = \pi/2$. **e**, Multiple attosecond pulses (pulse train), $\varphi_{CEP} = 0$. **f**, Multiple attosecond pulses (pulse train), $\varphi_{CEP} = \pi/2$. The lower plots in **a**–**f** show the respective pulse configurations at zero time

delay. The VIS pulse duration was 7 fs and the intensity was 3×10^{10} W cm^{-2}. **g**, **h**, Power spectral density distribution of the ΔA oscillation of the experiment (**g**) and the simulation (**h**). The frequency range used in the analysis is marked in red. We used the full modulation bandwidth, via filtering from near-zero frequency up to the Nyquist frequency, to retrieve the phase $\varphi_A(\tau)$.
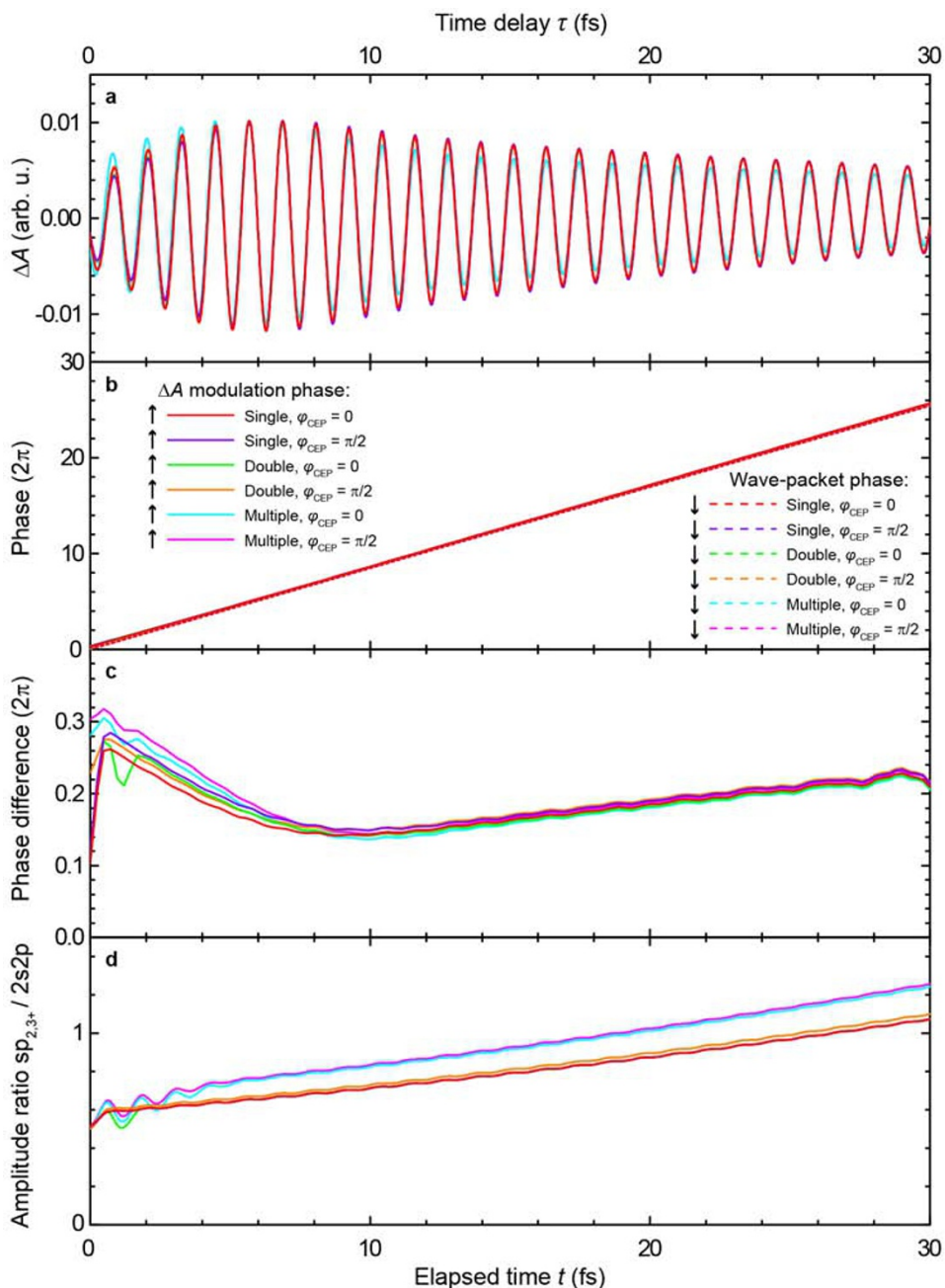
Extended Data Figure 6 | Reconstruction of the wave packet from time-delay-dependent $\Delta A(\tau)$ data near the $sp_{2,3+}$ resonance at 63.67 eV (simulation results). a, $\Delta A(\tau)$ for the different excitation scenarios shown in Extended Data Fig. 5. **b**, The phase $\varphi_A(\tau)$ extracted from the $\Delta A(\tau)$ oscillations (solid lines), compared with the phase $\varphi(t)$ of the wave packet (dashed lines) for the different excitation configurations. **c**, The difference between the (measurable) modulation phase $\varphi_A(\tau)$ and the wave-packet phase $\varphi(t)$ for each of the excitation scenarios. A time-delay-dependent correction phase of $\sim 0.4\pi$ needs to be taken into account to reconstruct the wave-packet phase $\varphi(t)$ in the experiment from the measured $\Delta A(\tau)$, as shown in Fig. 2. **d**, The variation in the wave-packet amplitude ratio for the different excitation configurations. Even in the extreme case of multiple attosecond pulses, the amplitude ratio is well defined within a region of $\pm 10\%$.
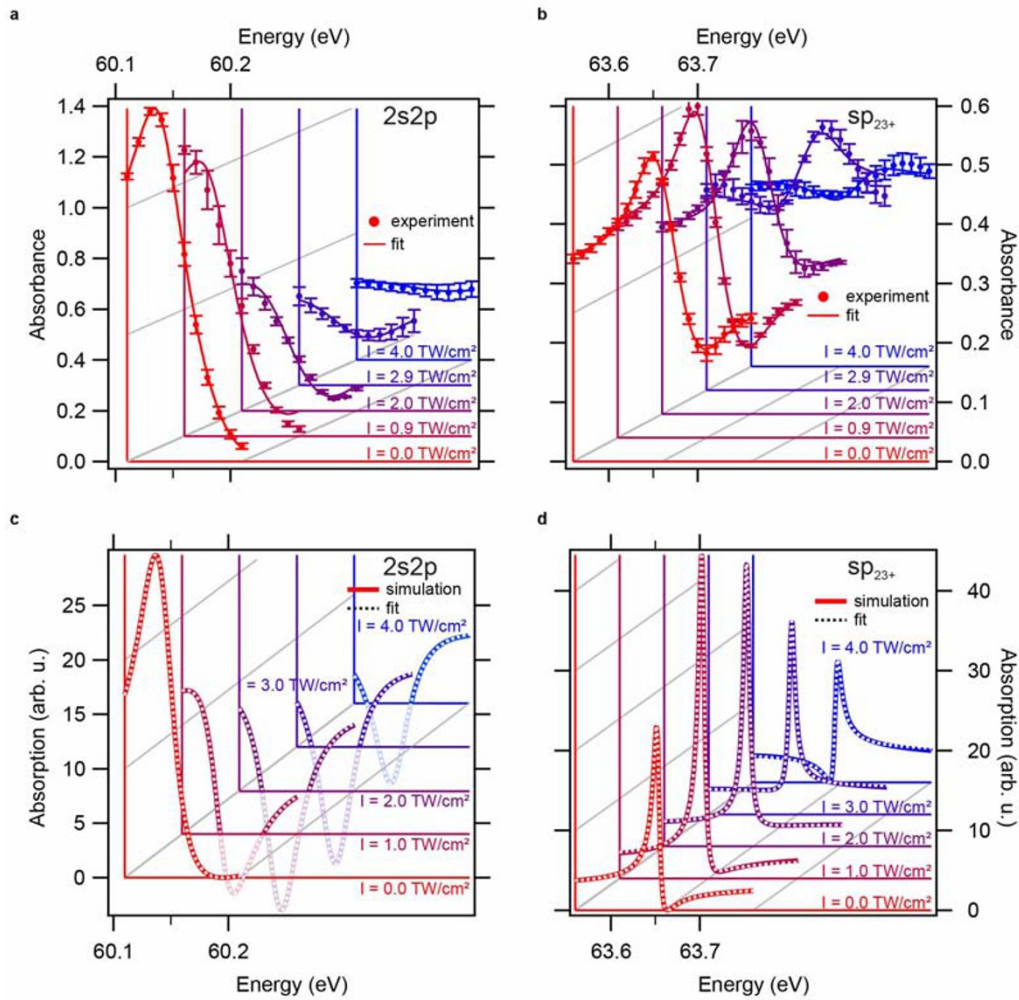
Extended Data Figure 7 | Fitting the intensity-dependent spectral line shapes of the 2s2p and the sp_{2,3+} resonances. **a, b**, Least-squares fit to the experimentally measured line shape shown in Fig. 4a. The laser-controlled line shape is shown for several laser intensities as given in the figure. Error bars here and phase error in Fig. 4c, d correspond to s.d. obtained by analysing at three values of $\tau = 5.35$ fs, $\tau = 4.15$ fs, $\tau = 6.55$ fs. **c, d**, Least-squares fit to the theoretically predicted line shape obtained from the *ab initio* simulation results shown in Fig. 4b, also plotted for several laser intensities as denoted in the figure. In all cases, the restricted energy region of the least-squares fit (2s2p, 60.11–60.21 eV (**a, c**); $sp_{2,3+}$, 63.56–63.76 eV (**b, d**)) ensures phase retrieval for times after the interaction with the laser pulse.